Intermetallics 112 (2019) 106542

Contents lists available at ScienceDirect

Intermetallics

journal homepage: www.elsevier.com/locate/intermet

Sublattice formation in CoCrFeNi high-entropy alloy

E.A. Meshkov[a,b,*], I.I. Novoselov[a,b], A.V. Shapeev[c], A.V. Yanilkin[a,b]

[a] Moscow Institute of Physics and Technology (State University), 141700, Moscow Region, Dolgoprydny, Institytski str. 9, Russian Federation
[b] Dukhov Research Institute of Automatics (VNIIA), 127055, Moscow, Syshevskaya str. 22, Russian Federation
[c] Skolkovo Institute of Science and Technology, Skolkovo Innovation Center, 43026, Moscow, Nobel str. 3, Russian Federation

ARTICLE INFO

Keywords:
High-entropy alloys
Order/disorder transformation
Multiscale
Monte carlo simulation
Ab-initio calculations

ABSTRACT

In this work, we investigated short-range ordering in the equiatomic CoCrFeNi high-entropy alloy by means of a machine-learning interatomic potential. The potential was represented as a low-rank tensor. The tensor coefficients were determined in order to reproduce the results of DFT calculations. This potential was used in an on-lattice Metropolis Monte-Carlo algorithm. We established, for the first time, that iron and chromium atoms form sublattices at the temperatures below 600°C and 1230°C, respectively.

1. Introduction

In 2004, Yeh [1] and Cantor [2] obtained pioneering results on multicomponent equiatomic metallic alloys. They showed that such alloys are able to form random solid solutions with highly symmetrical crystal lattices (FCC or BCC). Since then, this kind of compounds has drawn significant attention of scientific and engineering communities. These alloys contain at least four principle elements with concentrations between 5 and 35 at.%. This class of compounds is referred to as high-entropy alloys (HEA) due to large configurational entropy in comparison with conventional alloys. However, it has been shown [3–6] that configurational entropy does not always govern phase composition of HEAs. Other factors should also be considered, e.g., mixing enthalpy, vibrational and electronic entropy, etc. Several strategies have been proposed for prediction of phase composition of HEAs [7–14]. Nevertheless, none of these approaches are capable of accurate prediction of structures and phase compositions of HEAs.

The interest in HEAs is rapidly increasing due to outstanding properties of some of the investigated alloys [4]. For example, the equiatomic Cantor alloy CoCrFeMnNi exhibits a fine combination of mechanical properties such as extreme ductility [15,16], high tensile strength [17,18], hardness [19] and high fracture resistance at cryogenic temperatures [16,18]. Refractory MoNbTaVW has an almost constant yield strength at elevated temperatures [20]. $Al_{0.5}$CoCrCuFeNi has a high fatigue resistance [21] and both CoCrFeNiTi and AlCoCrFeNiTi have an excellent wear resistance [22]. Moreover, it was shown that the Cantor alloy and similar HEAs demonstrate high resistance to radiation-induced degradation processes such as swelling [23,24], hardening [24,25] and segregation [26].

CoCrFeNi (CCFN) is one of the most studied HEA. The phase composition of CCFN was investigated by standard (XRD) and energy-dispersive X-RAY (EDX), neutron diffraction and high-angle annular dark-field imaging (HAADF). In most of the works, it was demonstrated that CCFN forms a single-phase solid solution [14,27–29]. However, there are several experimental evidences of a more complex phase composition of CCFN. For instance, high-energy XRD analysis has shown the presence of two FCC lattices with close values of lattice constants [30]. Moreover, HAADF and EDX analysis has revealed precipitation of Cr atoms [31] and local ordering of Cr in CCFN [32].

CCFN was also extensively investigated by numerous theoretical approaches such as thermodynamic calculations (TC) [3,33], classical molecular dynamic (MD) [34,35], density functional theory [7,32,36], quantum MD (QMD) [37,38] and DFT coupled to Monte-Carlo (AIMC) [39]. However, the major drawbacks of these approaches are low accuracy in the case of TC, and small time and space scales for MD, QMD and AIMC. Therefore, a new approach capable of accurate prediction of HEA's phase composition is required. Ideally, the approach should combine the ability to cover large time and space scales with the accuracy of DFT. Good candidates are machine-learning techniques which have recently become popular in materials science [40–42].

In this work, we applied the low-rank potential [41] in the on-lattice formulation to investigate the thermodynamic stability of the CCFN solid solution in a wide range of temperatures.

* Corresponding author. Moscow Institute of Physics and Technology (State University), 141700, Moscow Region, Dolgoprydny, Institytski str. 9, Russian Federation.
E-mail address: meshkov@phystech.edu (E.A. Meshkov).

https://doi.org/10.1016/j.intermet.2019.106542
Received 8 February 2019; Received in revised form 3 June 2019; Accepted 10 June 2019

2. Computational details

Several types of computations were performed in this work. First, DFT calculations were carried out to create a database of configurations (see Section 2.1). Subsequently, the database was used to parametrize a machine-learning interatomic potential (see Section 2.2). Finally, the potential was embedded into the on-lattice Metropolis Mote-Carlo code [43] (see Section 2.3). The calculation details of each step are described in the following subsections.

2.1. Ab initio calculations

DFT calculations were performed using Vienna *Ab-Initio* Simulation Package (VASP) [44,45] with the projector augmented wave pseudopotentials [46,47]. The Perdew-Burke-Ernzerhof version of the generalized gradient approximation was used as the exchange-correlation functional [48]. The simulation cell contained 32 atoms that formed FCC lattice. Atoms were distributed randomly in the lattice sites. The plane-wave cut-off energy was set to 350 eV and the Monkhorst-Pack [49] k-point mesh of the size $3 \times 3 \times 3$ was used to achieve the 1 meV/atom convergence criterion. The Methfessel-Paxton technique [50] was applied for the reciprocal space energy integration. All the DFT calculations were performed at 0 K with relaxation of ions. Magnetic interactions were also accounted for. The details of the calculations of magnetic configurations are outlined in the Supplementary Materials.

FeNi and CoCrFeNi were investigated in this work. We created two databases for each of the systems: a training and a validation set. The training set was used for the parametrization of the machine-learning interatomic potential. The training set contained 200 and 2000 configurations for FeNi and CoCrFeNi, respectively. The validation set was used for the estimation of errors of the potential. The validation set contained 200 configurations for each system.

The configurations for both of the systems were generated in the following way. In order to represent random solid solution, constituent elements of the system were randomly distributed in the sites of FCC lattice structure. The concentration of each of the elements was in the range from 3 to 90%.

2.2. Machine-learning interatomic potential

We used the low-rank potential (LRP) representaion [41] in order to parametrize the DFT data. LRP belongs to a class of on-lattice machine-learning interatomic potentials. Application of LRP implies several assumptions. Firstly, it is proposed that atoms are located in the crystal lattice sites. Secondly, the total energy of the system (E_{total}) is represented as a sum of contributions of individual atomic environments (E_i):

$$E_{\text{total}} = \sum_{i=1}^{N} E_i, \tag{1}$$

where N is the number of atoms in the system. E_i is represented as a function of atomic types of the nearest neighbors of the i-th atom:

$$E_i = V(\sigma_1, .., \sigma_n), \tag{2}$$

where $\sigma_1, .., \sigma_n$ are the types of the nearest neighbors ($n = 12$ for the FCC lattice), $V(\sigma_1, .., \sigma_n)$ is the interatomic potential. Finally, $V(\sigma_1, .., \sigma_n)$ is assumed to have a low rank representation in the tensor-train format [41]. In other words, V has the following form:

$$V(\sigma_1, .., \sigma_n) = \prod_{i=1}^{n} A^{(i)}(\sigma_i), \tag{3}$$

which is a multiplication of tensors $A^{(i)}(\sigma_i)$ of different ranks. The maximum rank of $A^{(i)}(\sigma_i)$ was 12 in this work. The coefficients of the $A^{(i)}(\sigma_i)$ are found by minimization of the mean-squared error:

$$\frac{1}{K} \sum_{k=1}^{K} |E(\theta^{(k)}) - E^{\text{qm}}(\theta^{(k)})|^2, \tag{4}$$

where K is the number of configurations in the training set, $\theta^{(k)}$ is the k-th configuration, $E(\theta^{(k)})$ and $E^{\text{qm}}(\theta^{(k)})$ are the energies of the configuration predicted by LRP and DFT, respectively.

2.3. Monte-Carlo calculations

The SPPARKS simulation package [43] was used to perform on-lattice Metropolis Monte-Carlo calculations. The simulation cell contained 13500 FCC lattice sites and had the form of a cube with the length of an edge of 15 lattice periods or approximately 53 Å. Periodic boundary conditions were applied along the three dimensions.

For a given temperature, two types of the initial distribution of atoms were used for calculations: regular solid solutions and perfectly ordered systems. For the purpose of simulation we consider that the ordered FCC lattice consist of four simple cubic sublattices. Each of the sublattices was occupied by the atoms of the same type. The two initial conditions were used in order to verify that the systems achieved thermodynamic equilibrium. We assumed that the equilibrium was reached if the energies of both of the systems were close to each other during 10^3 swaps per atom, or more.

2.4. Short range order parameter

The Warren-Cowley short-range order (SRO) parameters [51] were used to assess the local degree of order. The SRO parameter $\alpha_{\text{A-B}}$ for the binary A–B system is defined by the following formula:

$$\alpha_{\text{A-B}} = 1 - \frac{P_{AB}}{c_{\text{B}}}, \tag{5}$$

where P_{AB} is the conditional probability of finding a B atom among the nearest neighbors of an atom A, c_{B} is the concentration of B atoms.

The correlation between the SRO parameter and the local distribution of atoms can be illustrated by the following examples. If an A atom is mostly surrounded by the atoms of the same type, then the P_{AB} is close to zero, and hence the SRO parameter is close to 1. If A and B atoms are distributed randomly, then the P_{AB} equals to c_{B} in Eq. (5), and the SRO parameter is close to zero. If an A atom is mostly surrounded by the atoms of the B type, then the SRO parameter has a negative value.

The SRO parameter in Eq. (5) is defined for a pair of elements. Therefore, an alloy with N component is characterized by the set of $\frac{N(N-1)}{2}$ SRO parameters, one for each pair of the components. Similarly to the case of binary systems, if $\alpha_{\text{A-B}}$ is close to zero in the multicomponent system then corresponding atoms form a random solid solution. A positive value represents the tendency for formation of clusters of A atoms, and a negative one indicates formation of intermetallic compounds.

Note that described behavior of $\alpha_{\text{A-B}}$ is true only if the A and B atoms have different types. In case of similar type of the atoms a positive value of SRO corresponds to formation of the sublattice, and a negative value indicates the presence of clusters in the system.

2.5. Validation of the LRP

LRP was validated by testing it on the binary FeNi system. We chose FeNi as the test system due to several reasons. Firstly, it contains the same elements as CCFN. Secondly, both FeNi and CCFN have FCC lattice symmetry. Finally, a large amount of experimental and theoretical data for FeNi is available in literature. Therefore, it can be used for verification of our results. Several tests were performed for FeNi in order to validate the applicability of LRP for the investigation of local ordering. First of all, the energies of the configurations from the validation set were calculated via LRP and DFT. The obtained data were used to determine the LRP energy errors. Secondly, the FeNi mixing

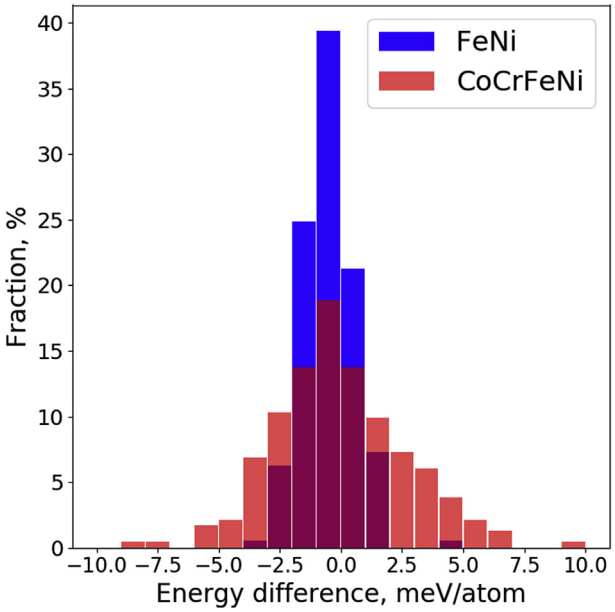

Fig. 1. Histogram of LRP energy errors with respect to DFT for FeNi (the blue bars) and CCFN (the red bars). The root-mean-square error for FeNi and CCFN is 1.2 and 2.8 meV/atom, respectively. (For interpretation of the references to colour in this figure legend, the reader is referred to the Web version of this article.)

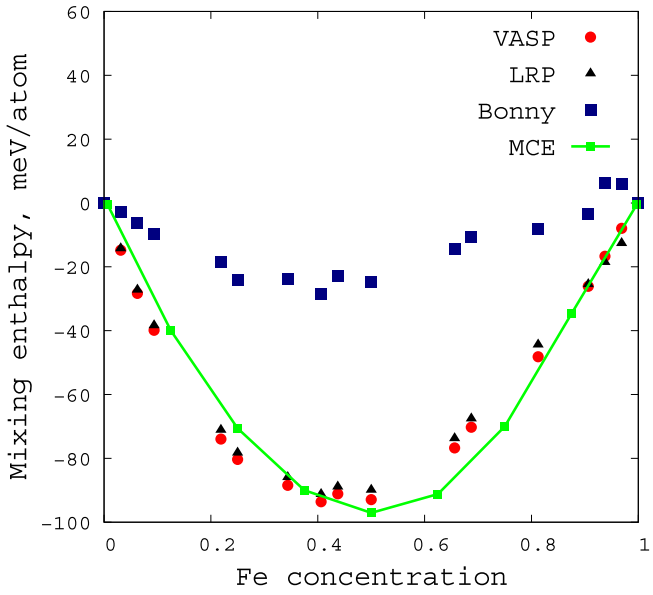

Fig. 2. The enthalpy of mixing of FeNi calculated from DFT (red circles), LRP (black triangles), Bonny EAM-potential (blue squares) [52] and magnetic cluster expansion (green squares) [53]. LRP is seen to correctly reproduce mixing enthalpy from DFT calculations. (For interpretation of the references to colour in this figure legend, the reader is referred to the Web version of this article.)

enthalpy was calculated via LRP and compared with the results of the DFT calculations. Finally, the order-disorder transition temperature of $FeNi_3$ was evaluated and compared with the experimental data. The main results of these tests are discussed below.

2.5.1. Comparison with ab initio calculations

Potential energies of the configurations from the FeNi and CCFN validation sets were computed via LRP and DFT. The histogram on Fig. 1 illustrates the resulting distribution of LRP errors with respect to DFT. The corresponding root-mean-square errors are 1.2 and 2.8 meV/atom for FeNi and CCFN, respectively. Therefore, it can be concluded that LRP accurately reproduces potential energies of binary and multicomponent alloys.

It should be noted that the values of the error we achieve with LRP is generally smaller than what is typically reported in literature for cluster expansion. For instance, for the refractory HEA MoNbTaVW the cluster expansion error was 8 meV/atom.

2.5.2. Mixing enthalpy of FeNi

Next we calculated the enthalpy of mixing of FeNi via LRP and DFT. The obtained results were compared with the existing data [7,52,53]. The enthalpy of mixing of an alloy was determined by following formula:

$$\Delta H^{\text{mix}} = E_{\text{alloy}} - \sum_{k=1}^{K} c_k E_k, \tag{6}$$

where E_{alloy} is the potential energy of an alloy, E_k is the energy value of the pure *k-th* component, c_K is the concentration of the *k-th* component in an alloy, K is the number of component in an alloy. It should be noted that constituent elements of FeNi (with FCC lattice) have different lattice structures (BCC and FCC for Fe and Ni, respectively). Therefore, in order to correctly compare mixing enthalpy with the results of other approaches [54], potential energy of Fe in FCC lattice structure was taken as potential energy of pure Fe.

Fig. 2 shows the compositional dependence of the mixing enthalpy of FeNi. The data was obtained via DFT, LRP and an EAM potential [52]. The results of magnetic cluster expansion (MCE) calculations [53] are also presented. Each point of the DFT and the LRP series was obtained by averaging over 15 different random solid solution configurations. It can be seen from Fig. 2 that LRP reproduces the enthalpy of mixing obtained in DFT calculations in the whole range of Fe concentrations. The agreement between the DFT and the MCE results is slightly worse. The EAM-potential reproduces the DFT data poorly.

The data for the equiatomic FeNi was used for quantitative comparison of the results. The mixing enthalpy of the alloy obtained with DFT [7] and MCE [53] equals to − 97 meV/atom. The enthalpy obtained in LRP and DFT calculations equals to − 90 and − 93 meV/atom, respectively. Thus, the LRP approach accurately predicts the values of mixing enthalpy for binary FeNi.

2.5.3. Order-disorder transition temperature of $FeNi_3$Lg

It is known that $FeNi_3$ has the phase transition from the ordered $L1_2$ structure to a random solid solution [55]. We employed the Warren-Cowley SRO parameter (Eq. (5)) in order to determine the order-disorder transition temperature of $FeNi_3$.

Fig. 3 illustrates the results of our calculations as well as the heat flow measured by differential scanning calorimetry (DSC) [55]. The experimental data suggests that the disordering begins at the onset temperature of 508°C. The heat flow reaches its maximum value of 1.2 W/g at the transition temperature of 609°C. In the LRP calculations, the ordering was investigated with the help of $\alpha_{\text{Fe-Fe}}$. The SRO parameter gradually rises with temperature up to 600°C. The further increase of temperature from 600 to 640°C leads to a significant raise of the SRO value. Finally, the order parameter remains almost constant at temperatures higher than 650°C. Hence, we conclude that the transition occurs between 600 and 640°C.

In order to determine the transition temperature more precisely, we analyzed the temperature dependence of the potential energy of the system. It can be seen from Fig. 3 that the SRO parameter correlates with the energy of the system. This correlation is expected for binary systems because both energy and SRO parameter are determined by local atomic environments. In order to determine the precise value of the transition temperature, the temperature derivative of the energy was calculated. The derivative has a sharp and narrow peak at 630°C

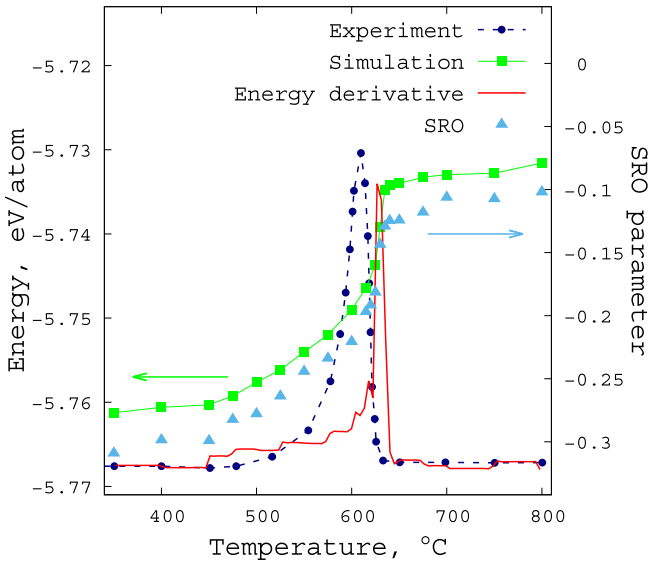

Fig. 3. Temperature dependence of the potential energy of the system (green squares), its derivative (red line), SRO parameter (teal triangles) from LRP calculations and the experimental values of DSC heat flow (blue circles) [55]. (For interpretation of the references to colour in this figure legend, the reader is referred to the Web version of this article.)

which corresponds to the transition temperature.

Fig. 4 demonstrates the variation of the potential energy of the system during calculations for three different temperatures. It can be seen that the energy of the system remains almost constant at 635°C. The analysis of the atomic positions in the simulation cell revealed that this behavior corresponds to the formation of a random solid solution. Similar behavior was observed at 625°C, but the solution is mostly ordered in this case.

In calculation at 630°C, the energy oscillates between the values obtained in computations at 625°C and 635°C. It means that the ordered regions are constantly formed and dissolved in the simulation cell. Indeed, the energy of the ordered $FeNi_3$ structure is lower then the energy of disordered one by 45 and 47 meV/atom in LRP and DFT calculations, respectively. The configurational entropy difference between these structures is 0,562 × R which is approximately 43 meV/atom at 630 °C.

These results support our conclusion that calculated order-disorder

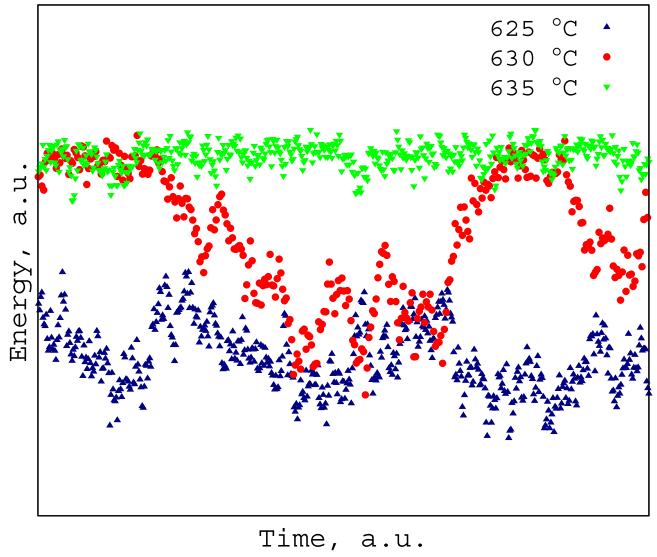

Fig. 4. System's energy variation during calculation at 625°C, 630°C and 635°C.

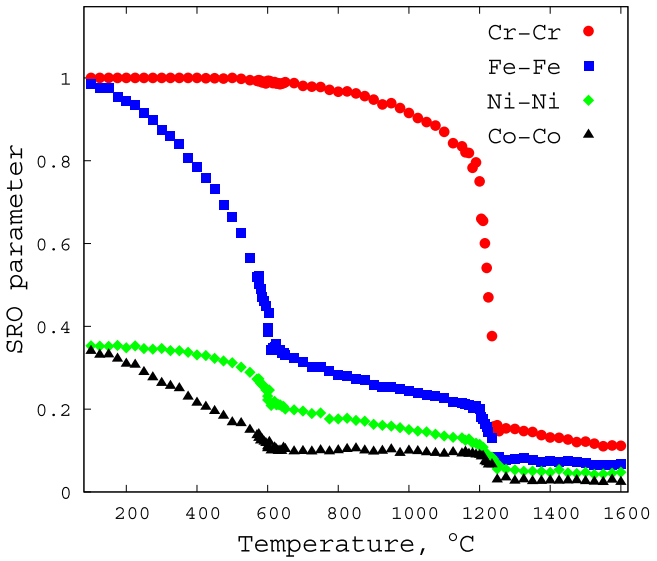

Fig. 5. Temperature dependence of SRO for different pairs of elements in CCFN.

transition temperature in $FeNi_3$ is close to 630°C. This value differs from the experimental one by only 20 K (or 1.7 meV/atom) which is comparable with the LRP error discussed in Section 2.5.1. In summary, LRP allows us to accurately reproduce the experimental data and the results of DFT calculations for FeNi.

3. Results and discussion

Ordering of CCFN was characterized by the α_{Cr-Cr}, α_{Fe-Fe}, α_{Ni-Ni} and α_{Co-Co} SRO parameters calculated for temperatures from 100°C to 1600°C. The corresponding data are shown on Fig. 5. It can be seen that the SRO parameter for Fe atoms decreases rapidly as the temperature increases to 600°C. After that, this parameter steadily goes down during the subsequent heating. The analysis of the atomic positions showed that this behavior corresponds to the disordering of a simple cubic sublattice of Fe atoms which is formed at temperatures below 300°C. To illustrate the formation of the sublattices, Fig. 6 shows a snapshot of the 5 × 5 × 5 area of the simulation cell with Fe (small blue spheres) and Cr (big red spheres) obtained at 200°C. Co and Ni atoms are not shown for clarity. It is clearly seen from the figure that Fe and Cr atoms form simple cubic sublattices. These sublattices steadily dissolve with

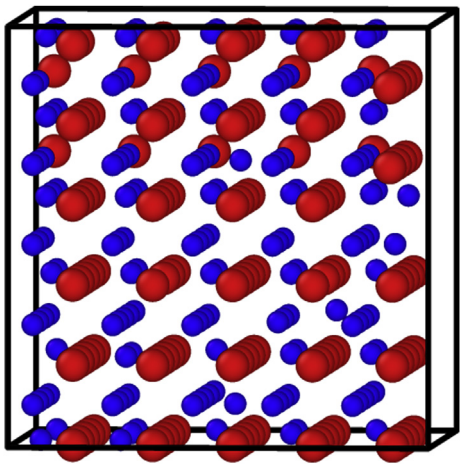

Fig. 6. The snapshot of the 5 × 5 × 5 area of the CCFN simulation cell with Fe and Cr sublattices at 200°C (small blue and big red spheres, respectively). (For interpretation of the references to colour in this figure legend, the reader is referred to the Web version of this article.)

temperature as it is shown on Fig. 5. The Fe sublattice disappears at 600°C. Further rise of temperature leads to a fairly random distribution of Fe atoms in the simulation cell. The subsequent decrease of the SRO parameter is attributed to dissolving of the Cr sublattice due to mutual dependence of all SRO parameters. As it is shown on Fig. 5, the α_{Cr-Cr} parameter has the profile similar to α_{Fe-Fe} in the whole temperature range. The Cr sublattice is stable up to 1230°C. The SRO parameters for Co and Ni atoms are lower than those for Fe and Cr atoms. This indicates that Co and Ni atoms are distributed relatively randomly in the simulation cell and do not form sublattices or clusters.

Additional DFT calculations have been performed in order to verify the LRP results. Particularly, the following types of configurations were considered: (i) random solid solution, (ii) chromium sublattice (Fe, Co, Ni atoms are distributed randomly in the FCC lattice sites), (iii) chromium and iron sublattices (Ni and Co atoms are distributed randomly in the FCC lattice sites). The calculations were performed via DFT for 50 different configurations for each of the three cases. As a result, the DFT calculations showed that the energies of (ii) and (iii) are lower than the energy of (i) by 72 and 96 meV/atom, respectively. LRP yields similar values of energies for these configurations, particularly 74 and 97 meV/atom, respectively. Therefore, the results of the DFT calculations confirm the conclusion that Fe and Cr atoms form sublattices in CCFN at low temperatures.

Similar results were obtained in Refs. [32,39] by means of DFT and DFT coupled with Monte-Carlo, respectively. In Ref. [32] it was demonstrated that the DFT calculations demonstrate that chromium atoms form an $L1_2$ structure (simple cubic sublattice). Ordering of other elements was not observed. However, the major drawback of calculations in this work is the small size of the simulation cell (120 atoms). Moreover, only individual configurations were considered in that paper, and the evolution of atomic structure was not studied.

In Ref. [39], Tamm et al. demonstrated that the ordering of iron and chromium atoms occurred in CCFN at temperatures up to 227°C and 927°C, respectively. However, the major drawback of this paper is also the small size of system (108 atoms). Moreover, only 2000 steps have been performed in the Monte-Carlo calculations [39] with only 18 swap trials per atom. Therefore, thermodynamic equilibrium might not have been achieved due to such a small number of swap trials. Finally, these Monte-Carlo calculations have been carried out for only three temperatures, which is not sufficient to accurately determine order-disorder transition temperature of the alloy. These drawbacks were avoided in the present work by numerous (85 different temperatures) long-time (10^4 swap trials per atom) calculations for large systems (13500 atoms).

Contradictory results were reported in the experimental studies of CCFN [29,32]. For instance, the formation of sublattices was not revealed by XRD and ND in Ref. [29]. On the other hand, the results of the HAADF investigation [32] suggested that the ordering of chromium atoms takes place. We estimated the number of atomic displacements during the preparation of the samples in the experiments [29,32]. For a given diffusion coefficient, the number of atomic displacements can be estimated as:

$$N_{jumps} = \frac{6Dt_{anneal}}{\Delta^2}, \quad (7)$$

where t_{anneal} is the annealing time, Δ is the distance between the nearest neighbors, D is a self-diffusion coefficient. The diffusion coefficient of Ni in CCFN was determined in Ref. [56]. This value was used as an estimation of the average self-diffusivity of CCFN. As a result, the numbers of displacements per atom are of the order of 10^7 and 10^9 for the annealing conditions employed in Refs. [29,32], respectively. It can be seen that the number of displacements per atom in Ref. [32] (the HAADF study) is 100 times greater than in Ref. [29] (the XRD study). Moreover, the microscopic HAADF investigation revealed only partial ordering of Cr atoms. Indeed, the small ordered domains were surrounded by a random solid solution. It means that even small ordered regions might not be formed due to the insufficient annealing time in Ref. [29].

Let us now compare the described results of the experiments with our findings. In general, the results of the LRP calculations qualitatively correspond to the HAADF findings. However, the obtained long-range ordering of Cr atoms (LRP) contradicts to the formation of small ordered domains (HAADF). This difference might be attributed to the change of magnetic contribution to total energy. Indeed, LRP reproduces the DFT energies obtained at absolute zero where magnetic interactions are strong. The magnetic contribution decreases significantly near the Curie temperature of CCFN which is approximately −140°C [57]. Therefore, the energy value at temperature from 100°C to 1600°C is expected to differ from the one from DFT calculations. This difference might change the long-range ordering of chromium atoms to the short-range one and decrease the melting temperature of the chromium sublattice.

As it was mentioned above, the phase composition of CCFN was investigated by diffraction techniques in Refs. [29,31]. Ordering of CCFN was not observed in these papers. It might be attributed to the fact that thermodynamic equilibrium was not reached during the samples preparation. Moreover, the registration of the sublattices could be challenging for the diffraction techniques even in the case of long-range ordering. To illustrate that, we performed a simulation of the XRD powder diffraction in the Mercury code [58]. The parameters of the simulation were chosen in accordance with the experimental values [29]: the wavelength of XRD was 1.7433 Å, the corresponding energy was 7.112 keV.

Fig. 7 illustrates the results of the simulation for the configuration with the Cr sublattice (other elements form random solid solution). It can be seen from Fig. 7 that the intensity of the sublattice peaks reaches only 0.5% of the intensity of the main FCC lattice peaks. The low intensity of the sublattice peaks is caused by the similarity of the values of Cr, Fe, Co and Ni form-factors. However, the noise level is approximately 4–5% of the intensity of the main peaks [29,31]. Therefore, the noise level is higher than the intensity of the sublattice peaks in XRD studies. On the other hand, the neutron scattering form-factors of CCFN elements differ significantly from each other. However, several ND experiments also did not reveal sublattice peaks [29,30]. These peaks might not be detected due to the low angular resolution of the experimental diffraction patterns. Hence, high-precision experiments with

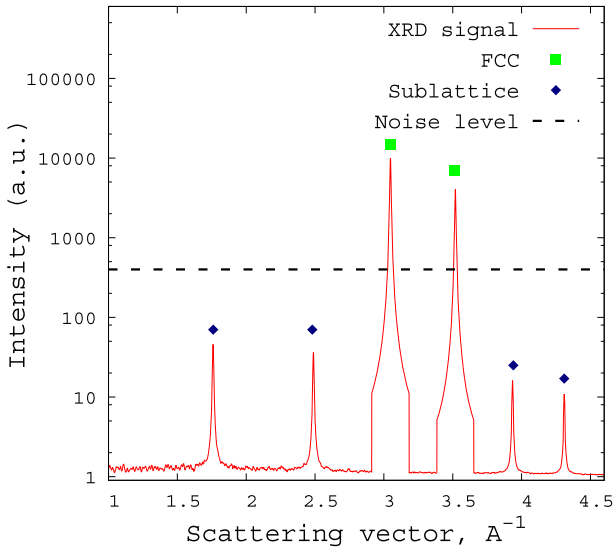

Fig. 7. XRD powder diffraction pattern of CCFN with Cr sublattice. Blue diamonds denote peaks associated to the sublattices. Green squares indicate the main peaks of the FCC lattice, dashed line is noise level estimated in Ref. [29]. (For interpretation of the references to colour in this figure legend, the reader is referred to the Web version of this article.)

a low noise level are required to detect ordering of CCFN by diffraction techniques.

4. Conclusions

In this work, we investigated a short range ordering in the CoCrFeNi high-entropy alloy in a wide range of temperatures. We employed LRP, a novel on-lattice machine-learning interatomic potential. The proposed approach was validated by the comparison with the results of DFT calculations and experimental data for binary FeNi. For CCFN, it was found that iron and chromium atoms form sublattices up to 600°C and 1230°C, respectively. The obtained results are consistent with the findings of other authors. In particular, the HAADF experiments on CCFN indicate the presence of the domains with ordered chromium atoms. On the other hand, the XRD studies suggest that CCFN is a random solid solution at 1000°C. However, the noise level of the XRD pattern is 4–5% and by an order of magnitude higher than the intensity of the sublattices peaks. The neutron diffraction studies also did not detect any sublattice peaks, possibly due to insufficient angular resolution of the experimental diffraction patterns. Thus, further theoretical and experimental investigations are required in order to understand the ordering behavior of CCFN.

Acknowledgments

This work was supported by the Russian Science Foundation (grant number 18-13-00479).

Appendix A. Supplementary data

Supplementary data to this article can be found online at https://doi.org/10.1016/j.intermet.2019.106542.

References

[1] J.-W. Yeh, S.-K. Chen, S.-J. Lin, J.-Y. Gan, T.-S. Chin, T.-T. Shun, C.-H. Tsau, S.-Y. Chang, Nanostructured high-entropy alloys with multiple principal elements: novel alloy design concepts and outcomes, Adv. Eng. Mater. 6 (5) (2004) 299–303.
[2] B. Cantor, I. Chang, P. Knight, A. Vincent, Microstructural development in equiatomic multicomponent alloys, Mater. Sci. Eng. A 375–377 (2004) 213–218 https://doi.org/10.1016/j.msea.2003.10.257.
[3] D. Miracle, O. Senkov, A critical review of high entropy alloys and related concepts, Acta Mater. 122 (2017) 448–511 https://doi.org/10.1016/j.actamat.2016.08.081.
[4] E.J. Pickering, N.G. Jones, High-entropy alloys: a critical assessment of their founding principles and future prospects, Int. Mater. Rev. 61 (3) (2016) 183–202, https://doi.org/10.1080/09506608.2016.1180020.
[5] F. Otto, Y. Yang, H. Bei, E. George, Relative effects of enthalpy and entropy on the phase stability of equiatomic high-entropy alloys, Acta Mater. 61 (7) (2013) 2628–2638 https://doi.org/10.1016/j.actamat.2013.01.042.
[6] O. Senkov, J. Miller, D. Miracle, C. Woodward, Accelerated exploration of multi-principal element alloys for structural applications, Calphad 50 (2015) 32–48 https://doi.org/10.1016/j.calphad.2015.04.009.
[7] M. Troparevsky, J. Morris, P. Kent, A. Lupini, G. Stocks, Criteria for predicting the formation od single-phase high-entropy alloys, Phys. Rev. X 5.
[8] O. Senkov, D. Miracle, A new thermodynamic parameter to predict formation of solid solution or intermetallic phases in high entropy alloys, J. Alloy. Comp. 658 (2016) '603–607'.
[9] Y. Ye, J. wang, J. Lu, C. Liu, Y. Yang, Design of high entropy alloys: a single-parameter thermodynamic rule, Scripta Mater. 104 (2015) '53–55'.
[10] I. Toda-Caraballo, P. Rivera-Díaz-del Castillo, A criterion for the formation of high entropy alloys based on lattice distortion, Intermetallics 71 (2016) '76–87'.
[11] D. King, S. Middleburgh, A. McGregor, M. Cortie, Prediction the formation and stability of single-phase high-entropy alloys, Acta Mater. 104 (2016) '172–179'.
[12] Z. Leong, J. Wróbel, S. Dudarev, R. Goodall, I. Todd, D. Nguyen-Manh, The effect of electronic structure on the phases present in high entropy alloys, Sci. Rep. 7.
[13] N. Yurchenko, N. Stepanov, G. Salishchev, Laves-phase formation criterion for high-entropy alloys, Mater. Sci. Technol. 33 (1) (2017) '17–22'.
[14] M.-H. Tsai, J.-H. Li, A.-C. Fan, P.-H. Tsai, Incorrect predictions of simple solid solution high entropy alloys: cause and possible solution, Scripta Mater. 127 (2017) 6–9 https://doi.org/10.1016/j.scriptamat.2016.08.024.
[15] G. Salishchev, M. Tikhonovsky, D. Shaysultanov, N. Stepanov, A. Kuznetsov, I. Kolodiy, A. Tortika, O. Senkov, Effect of mn and v on structure and mechanical properties of high-entropy alloys based on cocrfeni system, J. Alloy. Comp. 591 (2014) 11–21 https://doi.org/10.1016/j.jallcom.2013.12.210.
[16] A. Gali, E. George, Tensile properties of high- and medium-entropy alloys, Intermetallics 39 (2013) 74–78 https://doi.org/10.1016/j.intermet.2013.03.018.
[17] M. Kang, J.W. Won, J.B. Kwon, Y.S. Na, Intermediate strain rate deformation behavior of a cocrfemnni high-entropy alloy, Mater. Sci. Eng. A 707 (2017) 16–21 https://doi.org/10.1016/j.msea.2017.09.026.
[18] B. Gludovatz, A. Hohenwarter, D. Catoor, E.H. Chang, E.P. George, R.O. Ritchie, A fracture-resistant high-entropy alloy for cryogenic applications, Science 345 (6201) (2014) 1153–1158, https://doi.org/10.1126/science.1254581.
[19] A.J. Zaddach, C. Niu, C.C. Koch, D.L. Irving, Mechanical properties and stacking fault energies of nifecrcomn high-entropy alloy, JOM 65 (12) (2013) 1780–1789, https://doi.org/10.1007/s11837-013-0771-4.
[20] O. Senkov, G. Wilks, J. Scott, D. Miracle, Mechanical properties of $nb_{25}mo_{25}ta_{25}w_{25}$ and $v_{25}nb_{20}mo_{20}ta_{20}w_{20}$ refractory high entropy alloys, Intermetallics 19 (5) (2011) 698–706.
[21] M. Hemphill, T. Yuan, G. Wang, J. Yeh, C. Tsai, A. Chuang, P. Liaw, Fatigue behavior of $al_{0.5}$cocrcufeni high entropy alloys, Acta Mater. 60 (2012) 57235734 https://doi.org/10.1016/j.actamat.2012.06.046.
[22] M.-H. Chuang, M. Tsai, W.-R. Wang, S.-J. Lin, J.-W. Yeh, Microstructure and wear behavior of $al_xco_{1.5}crfeni_{1.5}ti_y$ high-entropy alloys, Acta Mater. 59 (16) (2011) 6308–6317 https://doi.org/10.1016/j.actamat.2011.06.041.
[23] C. Lu, L. Niu, N. Chen, K. Jin, T. Yang, P. Xiu, Y. Zhang, F. Gao, H. Bei, S. Shi, M.-R. He, I.M. Robertson, W.J. Weber, L. Wang, Enhancing radiation tolerance by controlling defect mobility and migration pathways in multicomponent single-phase alloys, Nat. Commun. 7 (2016) 13564 (EP –, article).
[24] K. Jin, C. Lu, L. Wang, J. Qu, W. Weber, Y. Zhang, H. Bei, Effects of compositional complexity on the ion-irradiation induced swelling and hardening in ni-containing equiatomic alloys, Scripta Mater. 119 (2016) 65–70 https://doi.org/10.1016/j.scriptamat.2016.03.030.
[25] C. Hofer, E. Stergar, S. Maloy, Y. Wang, P. Hosemann, An intermetallic forming steel under radiation for nuclear applications, J. Nucl. Mater. 458 (2015) 361–368 https://doi.org/10.1016/j.jnucmat.2014.12.099.
[26] C. Lu, T. Yang, K. Jin, N. Gao, P. Xiu, Y. Zhang, F. Gao, H. Bei, W.J. Weber, K. Sun, Y. Dong, L. Wang, Radiation-induced segregation on defect clusters in single-phase concentrated solid-solution alloys, Acta Mater. 127 (2017) 98–107 https://doi.org/10.1016/j.actamat.2017.01.019.
[27] Y. Brif, M. Thomas, I. Todd, The use of high-entropy alloys in additive manufacturing, Scripta Mater. 99 (2015) 93–96 https://doi.org/10.1016/j.scriptamat.2014.11.037.
[28] F. He, Z. Wang, Q. Wu, J. Li, J. Wang, C. Liu, Phase separation of metastable cocrfeni high entropy alloy at intermediate temperatures, Scripta Mater. 126 (2017) 15–19 https://doi.org/10.1016/j.scriptamat.2016.08.008.
[29] M. Lucas, G. Wilks, L. Mauger, J.A. Munoz, O. Senkov, E. Michel, J. Horwath, S. Semiatin, M.B. Stone, D.L. Abernathy, et al., Absence of long-range chemical ordering in equimolar fecocrni, Appl. Phys. Lett. 100 (25) (2012) 251907.
[30] U. Dahlborg, J. Cornide, M. Calvo-Dahlborg, T. Hansen, A. Fitch, Z. Leong, S. Chambreland, R. Goodall, Structure of some cocrfeni and cocrfenipd multi-component hea alloys by diffraction techniques, J. Alloy. Comp. 681 (2016) 330–341 https://doi.org/10.1016/j.jallcom.2016.04.248.
[31] K. Christofidou, E. Pickering, P. Orsatti, P. Mignanelli, T. Slater, H. Stone, N. Jones, On the influence of mn on the phase stability of the crmnxfeconi high entropy alloys, Intermetallics 92 (2018) 84–92 https://doi.org/10.1016/j.intermet.2017.09.011.
[32] C. Niu, A. Zaddach, A. Oni, X. Sang, J. Hurt III, J. LeBeau, C. Koch, D. Irving, Spin-driven ordering of cr in the equiatomic high entropy alloy nifecrco, Appl. Phys. Lett. 106 (16) (2015) 161906.
[33] C. Zhang, F. Zhang, S. Chen, W. Cao, Computational thermodynamics aided high-entropy alloy design, JOM 64 (7) (2012) 839–845, https://doi.org/10.1007/s11837-012-0365-6.
[34] S.-W. Kao, J.-W. Yeh, T.-S. Chin, Rapidly solidified structure of alloys with up to eight equal-molar elementsa simulation by molecular dynamics, J. Phys. Condens. Matter 20 (14) (2008) 145214.
[35] G. Anand, R. Goodall, C.L. Freeman, Role of configurational entropy in body-centred cubic or face-centred cubic phase formation in high entropy alloys, Scripta Mater. 124 (2016) 90–94 https://doi.org/10.1016/j.scriptamat.2016.07.001.
[36] D. Ma, B. Grabowski, F. Krmann, J. Neugebauer, D. Raabe, Ab initio thermodynamics of the cocrfemnni high entropy alloy: importance of entropy contributions beyond the configurational one, Acta Mater. 100 (2015) 90–97 https://doi.org/10.1016/j.actamat.2015.08.050.
[37] L. Santodonato, Y. Zhang, M. Feygenson, C. Parish, M. Gao, R. Weber, J. Neuefeind, Z. Tang, P. Liaw, Deviation from high-entropy configurations in the atomic distributions of a multi-principal-element alloy, Nat. Commun. 6 (2015) 5964.
[38] M.C. Gao, D.E. Alman, Searching for Next Single-phase High-Entropy Alloy Compositions, (2013), pp. 4504–4519, https://doi.org/10.3390/e15104504.
[39] A. Tamm, A. Aabloo, M. Klintenberg, M. Stocks, A. Caro, Atomic-scale properties of ni-based fcc ternary, and quaternary alloys, Acta Mater. 99 (2015) 307–312 https://doi.org/10.1016/j.actamat.2015.08.015.
[40] N. Castin, L. Messina, C. Domain, R.C. Pasianot, P. Olsson, Improved atomistic Monte Carlo models based on ab-initio-trained neural networks: application to fecu and fecr alloys, Phys. Rev. B 95 (2017) 214117, https://doi.org/10.1103/PhysRevB.95.214117.
[41] A. Shapeev, Accurate representation of formation energies of crystalline alloys with many components, Comput. Mater. Sci. 139 (2017) 26–30 https://doi.org/10.1016/j.commatsci.2017.07.010.
[42] D. Dragoni, T.D. Daff, G. Csányi, N. Marzari, Achieving dft accuracy with a machine-learning interatomic potential: thermomechanics and defects in bcc ferromagnetic iron, Phys. Rev. Mater. 2 (2018) 013808, , https://doi.org/10.1103/PhysRevMaterials.2.013808.

[43] A. Slepoy, A. Thompson, S. Plimpton, A constant-time kinetic monte-carlo algorithm for simulation of large biochemical reaction networks, J. Chem. Phys. 128 (205101) (2008) 1–9.
[44] G. Kresse, J. Furthmuller, Efficiency of ab-initio total energy calculations for metals and semiconductors using a plane-wave basis set, Comput. Mater. Sci. 6.
[45] J. Furtmuller, G. Kresse, Efficient iterative schemes for *ab initio* total-energy calculations using a plane-wave basis set, Phys. Rev. B 54 (16) (1996) 11169–11186.
[46] G. Kresse, D. Joubert, From ultrasoft pseudopotentials to the projector augmented-wave method, Phys. Rev. B. 59 (1999) 31758–31775.
[47] P. Blochl, Projector augmented-wave method, Phys. Rev. B. 50 (24) (1994) 17953–17979.
[48] J. P. K. B. M. Ernzerhof, Generalized gradient approximation made simple, Phys. Rev. Lett. 77 (3865).
[49] H. Monkhorst, J. Pack, Special points for brillouin-zone integration, Phys. Rev. B 13.
[50] M. Methfessel, A. Paxton, High-precision sampling for brillouin-zone integration in metals, Phys. Rev. B 40 (6) (1989) '3616–3621'.
[51] J. Cowley, Short- and long-range order parameters in disordered solid solutions, Phys. Rev. 120 (5) (1960) 1648–1657.
[52] G. Bonny, R. Pasianot, L. Malerba, Fe–ni many-body potential for metallurgical applications, Model. Simul. Mater. Sci. Eng. 17 (2) (2009) 025010.
[53] M. Lavrentiev, J. Wrobel, D. Nguyen-Manh, S. Dudarev, Magnetic and thermodynamic properties of face-centered cubic fe-ni alloys, Phys. Chem. Chem. Phys. 30 (2014) '16049–16059'.
[54] C. Niu, A. Zaddach, C. Koch, D. Irving, First principles exploration of near-equiatomic nifecrco high entropy alloys, J. Alloy. Comp. 672 (2016) 510–520 https://doi.org/10.1016/j.jallcom.2016.02.108.
[55] J. Liu, L. Riddiford, C. Floristean, F. Goncalves-Neto, M. Rezaeeyazdi, L. Lewis, K. Barmak, Kinetics of order-disorder transformation of $l1_2 feni_3$ in the fe-ni system, J. Alloy. Comp. 689 (2016) 593–598.
[56] M. Vaidya, S. Trubel, B. Murty, G. Wilde, S. Divinski, Ni tracer diffusion in cocrfeni and cocrfemnni high entropy alloys, J. Alloy. Comp. 688 (2016) '994–1001'.
[57] M.S. Lucas, D. Belyea, C. Bauer, N. Bryant, E. Michel, Z. Turgut, S.O. Leontsev, J. Horwath, S.L. Semiatin, M.E. McHenry, C.W. Miller, Thermomagnetic analysis of fecocrxni alloys: magnetic entropy of high-entropy alloys, J. Appl. Phys. 113 (17) (2013) 17A923, https://doi.org/10.1063/1.4798340.
[58] C. Macrae, I. Bruno, J. Chisholm, P. Edgington, P. McCabe, E. Pidcock, L. Rodriguez-Monge, J. Taylor, R. van de Streek, P. Wood, Mercury csd 2.0 - new features for visualization and investigation of crystal structures, J. Appl. Crystallogr. 41 (2008) '466–470'.